Nacre-inspired magnetically oriented micro-cellulose fibres/ nano-hydroxyapatite/chitosan layered scaffold enhances pro-osteogenesis and angiogenesis

Yu-Wei Ge [a,1], Min Chu [b,1], Zi-Yang Zhu [a,1], Qin-Fei Ke [b], Ya-Ping Guo [b,***], Chang-Qing Zhang [a,**], Wei-Tao Jia [b,*]

[a] *Department of Orthopedic Surgery, Shanghai Jiao Tong University Affiliated Sixth People's Hospital, Shanghai, 200233, China*
[b] *The Education Ministry Key Lab of Resource Chemistry and Shanghai Key Laboratory of Rare Earth Functional Materials, Shanghai Normal University, Shanghai, 200234, China*

ABSTRACT

In situ regeneration of large-segment bone defects is a difficult clinical problem. Here, we innovatively developed magnetically oriented micro-cellulose fibres using nano-hydroxyapatite/chitosan (CEF/Fe$_3$O$_4$/HA/CS) and loaded an NFκB pathway inhibitor on the surface of magnetically oriented cellulose fibres (CEF/Fe$_3$O$_4$/HA/CS/PQQ) prepared as a layered bioscaffold. CEF/Fe$_3$O$_4$/HA/CS/PQQ was constructed by layering HA/CS sheets. Nano-hydroxyapatite was deposited on the surface of cellulose fibres, then the magnetic nanoparticles on the cellulose fibres were aligned on the surface of chitosan under a magnetic field. Oriented cellulose fibres enhanced the compressive properties of the scaffold, with an average maximum compressive strength of 1.63 MPa. The CEF/Fe$_3$O$_4$/HA/CS/PQQ layered scaffold was filled into the body, and the acute inflammatory response (IL-1β and TNF-α) was suppressed through the early sustained release of PQQ. The CEF/Fe$_3$O$_4$/HA/CS/PQQ-layered scaffold further inhibited the osteoclasts differentiation. It was further found that the nano-hydroxyapatite on the surface of oriented cellulose fibres promoted the formation and migration of new blood vessels, accelerated the processing of collagen-I fibres to cartilage, and endochondral ossification. Hence, the development of the CEF/Fe$_3$O$_4$/HA/CS/PQQ layered scaffold with oriented fibres guides bone growth direction and pro-osteogenesis activity and provides a novel strategy for the *in situ* regeneration of large segmental bone defects.

1. Introduction

In recent years, bone tissue defects caused by orthopaedic diseases, traffic accidents, and osteoporosis have posed significant challenges to using biomedical materials [1–4]. Owing to the limitations of autologous and allogeneic bone and the occurrence of complications during bone surgery, research on alternative materials for bone repair is particularly urgent [2,5,6]. Bone defect repair materials have gone through three generations of development [7,8]. The first generation of these materials comprises bioinert materials, divided into metal [9], ceramic [10] and synthetic polymer [11] materials. The second-generation bone repair materials are bioactive materials, including polyester, collagen, calcium

phosphate [12] and bioactive glass [13], Finally, third-generation materials, defined as smart materials, are both bioactive and biodegradable [14,15]. Although third-generation bone repair materials have been developed, they still have shortcomings. First, their mechanical properties are not as strong as those of natural bone. The special structure and composition of the extracellular matrix in the bone play an important role in its strength. Second, third-generation bone repair materials can still cause an early acute inflammatory response, inhibit angiogenesis, and promote fibrous tissue proliferation.

Normal bone tissue contains osteoblasts, osteocytes and osteoclasts, as well as extracellular matrix components (collagen fibers and nano-hydroxyapatite [16,17]). Collagen fibers showed a regular

arrangement, and at the same time, nano-hydroxyapatite was also attached to the collagen fibers. Together they organize an important part of the haversian canal [18,19]. Therefore, the research of bone biomimetic materials has always been a great challenge [20]. It has been found that the toughness of materials can be enhanced by the introduction of shear force or fibres [21,22]. Fibre orientation affects the properties of scaffolds in several ways [18]. Ramon et al. found that fibre orientation had a significant impact on cell morphology and orientation and that cells were arranged along the fibre direction of the scaffold to form spindle shapes parallel to the scaffold fibre [23]. Wang et al. found that cells on randomly oriented scaffolds were irregularly shaped, cells on parallel scaffolds had a fender shape, and cells grown on super-parallel scaffolds had a large length-diameter ratio along the fibre direction [24]. Accardi MA et al. studied the mechanical and frictional properties of scaffolds with different fibre orientations. They found that fibre orientations strongly influenced the tensile properties and compression modulus of scaffolds, while they had no significant effect on the equilibrium friction coefficient. Moreover, they found that the fibre orientations of scaffolds implanted in joints strongly influenced their ability to resist shear damage [25]. Hence, they concluded that fibre-oriented scaffolds not only enhanced the mechanical properties of scaffolds but also affected the arrangement, growth, and morphology of cells [26].

There are many ways to orient fibres. Some researchers have used fluid shear stress to promote fibre orientation [21,27]. Electrostatic spinning is commonly used to promote fibre orientation [26,28,29]. Inspired by the brick-and-mortar structures of nacre in nature, the layers are interconnected by a biopolymer matrix [30–33]. Based on previous studies, we prepared hydroxyapatite/chitosan layered scaffolds reinforced with magnetically oriented cellulose fibres by combining magnetic field and freeze-drying. Hydroxyapatite/chitosan layered scaffolds mimic the nacre structure [34]. The microstructure of the shell nacre is composed of layers of calcium carbonate and organic matter, and has good mechanical properties [35–37]. The cellulose fibres were first modified to be loaded with magnetic ferric oxide nanoparticles, and a hydroxyapatite layer was then deposited on them. The composite fibres were then aligned in the scaffolds under the action of an external magnetic field.

Furthermore, while considering mechanical strength, we also developed a plan for an acute inflammatory response. Pyrroloquinoline quinone (PQQ) is a natural antioxidant [38] with antiaging properties [39]. Recently, PQQ was reported to regulate multiple intracellular signalling pathways, including the RANKL-mediated c-Fos/NFATc1 pathway [40]; activation of the Ras pathway [41], and CREB-dependent mitochondrial production [42]. The reported anti-inflammatory effects of PQQ mostly focused on the treatment of microglia [43], acute liver injury [44] and acute spinal cord injury [39], and studies have found that PQQ plays a role in inhibiting the NF-κB signalling pathway [40]. The NF-κB signalling pathway plays a key role in the acute inflammatory response. The release of pro-inflammatory factors such as IL-1β and TNF-α is also accomplished through this signalling pathway. Our research group loaded PQQ on magnetically oriented cellulose fibres and deposited nano-hydroxyapatite on these fibres, improving the strength of the fibres and the loading rate.

Mimicking the hierarchical structure of nacre is a promising approach to obtain high mechanical properties. In this work, nacre-inspired layered CEF/Fe$_3$O$_4$/HA/CS/PQQ scaffolds have great potential for applications in bone tissue engineering. The ultimate purpose of this experiment was to investigate the mechanical properties of CEF/Fe$_3$O$_4$/HA/CS/PQQ layered scaffolds, and how they promote the formation of new blood vessels, promote osteogenic ability, and inhibit the early inflammatory response. By simulating the composition of human bone tissue (collagen fibres and hydroxyapatite longitudinally arranged in parallel) and inspired by the layered properties of nacre, we fabricated CEF/Fe$_3$O$_4$/HA/CS/PQQ layered scaffolds with oriented structures for the first time using a combination of freeze-drying and biomineralisation methods. We also verified that CEF/Fe$_3$O$_4$/HA/CS/PQQ layered scaffolds

inhibited the acute inflammatory response and inflammation-mediated bone homeostasis caused by osteoclast hyperactivity and promoted neovascularisation and new bone tissue formation *in vivo* and *in vitro*.

2. Materials and methods

2.1. Materials

Cellulose-Fiber (CEF), model for F-01, 60 mm, was obtained from the Shanghai Key Laboratory of Rare Earth Functional Materials. FeCl$_2$·4H$_2$O (98%) was purchased from Alfa Aesar Chemical Co., Ltd. (Shanghai, China). FeCl$_3$·6H$_2$O (99%) was obtained from Titan Scientific Co. Ltd. (Shanghai, China). Ca(NO$_3$)$_2$ (AR ≥99.8%) and chitosan were purchased from Aladdin Reagent Co., Ltd. (Shanghai, China). NaOH was obtained from Sinopharm Chemical Reagent Co., Ltd. NH$_3$·H$_2$O (25–28%) was purchased from Shanghai Maclin Biochemical Technology Co., Ltd. Genipin (98%) was obtained from the Letter Biotechnology Company.

2.2. Preparation of CEF/Fe$_3$O$_4$

To prepare CEF/Fe$_3$O$_4$, FeCl$_2$·4H$_2$O:FeCl$_3$·6H$_2$O = 1.25:2, 0.622 g FeCl$_2$·4H$_2$O, and 1.359 g FeCl$_3$·6H$_2$O were dissolved in 20 mL of deionised water. Separately, 1 g CEF was added to 20 mL deionised water and stirred with a magnetic stirrer. The prepared FeCl$_2$·4H$_2$O:FeCl$_3$·6H$_2$O solution was slowly dropped into the cellulose fibre solution using a separatory funnel, and 14% NH$_3$·H$_2$O was added simultaneously to ensure the pH of the solution was approximately 9. A large amount of black precipitate was generated at room temperature, so the resulting solution was heated at 60 °C for 45 min. The heated solution was then pumped and filtered, deionised water and ethanol were used to wash the precipitate to a neutral pH, and the precipitate was dried in an oven at 30 °C to prepare cellulose fibres loaded with Fe$_3$O$_4$ particles.

2.3. Preparation of CEF/Fe$_3$O$_4$/HA

CEF/Fe$_3$O$_4$/HA was prepared using a chemical co-precipitation method. Briefly, 80 mL 0.1 mol/L Ca(NO$_3$)$_2$ solution and 96 mL 0.1 mol/L sodium phosphate solution were prepared. The pH of the Ca(NO$_3$)$_2$ solution was adjusted to 10 using NaOH. Then, 1 g CEF was added to the mix and was mixed well. The sodium phosphate solution was then slowly dropped into the Ca(NO$_3$)$_2$ solution at room temperature and stirred for 2 h. The resulting solution was then pumped and dried at 30 °C.

2.4. Preparation of CEF/Fe$_3$O$_4$/HA/CS scaffold

To prepare the scaffolds, 0.8 g chitosan powder was added to 40 mL 1% acetic acid solution, stirred and heated in a 37 °C water bath to form 2% chitosan acetic acid solution. Composite fibres (0.5 g) were added to the chitosan acetic acid solution under magnetic stirring. Then, 2 mL 1% genipin solution was dropped into the chitosan solution, continuously stirred, and allowed to crosslink for 1 h. Then, a cuboid mould was subjected to a magnetic field, glued at 4 °C for 1 h, frozen at −20 °C for 12 h, and then freeze-dried at −60 °C for 24 h. The dried materials were then soaked in 10% NaOH solution for 24 h, washed to neutral pH with deionised water, and freeze-dried again for another 24 h to prepare the scaffold material.

2.5. Preparation of CEF/Fe$_3$O$_4$/HA/CS/PQQ scaffold

Here, 0.8 g chitosan powder was added to 40 mL 1% acetic acid solution, stirred, and heated in a 37 °C water bath to form a 2% chitosan acetic acid solution. Composite fibres (0.5 g) were then added to the chitosan acetic acid solution under magnetic stirring. Next, 132 μL of pyrrorole quinolaquin (PQQ) solution and 2 mL 1% genipin solution were added, continuously stirred, and allowed to crosslink for 1 h. Then,

a cuboid mould was subjected to a magnetic field, glued at 4 °C for 1 h, frozen at −20 °C for 12 h, and then freeze-dried at −60 °C for 24 h. The dried scaffolds were then soaked in 10% NaOH solution for 24 h, washed to neutral pH with deionised water, and freeze-dried again for 24 h to prepare the final scaffold material.

2.6. Characterization

Scanning electron microscopy was used to observe the surface morphology and elemental distribution of the CS, CEF/Fe$_3$O$_4$/HA/CS, and CEF/Fe$_3$O$_4$/HA/CS/PQQ layered scaffolds (field emission scanning electron microscope; Hitachi S-4800, Hitachi Manufacturing Co., Ltd.). The chemical composition of the scaffold was determined using an energy-dispersive spectrometer (EDS). An X-ray diffractometer was also used (D/MAX-III, Japan), with Cu-Kα as the radiation source (λ = 1.541874 Å), at an angle of 2θ = 10–60°, a scanning rate of 5°/min, a voltage of 40 V, and a current of 50 mA. A Fourier infrared instrument (Frontier, PerkinElmer, USA) was used at wavenumbers between 500 and 4000 cm^{-1}, resolution of 4 cm^{-1}, and test voltage of 100–230 V. An electronic universal testing machine (WDW, 20C) was used to measure the mechanical properties of the scaffolds. Each sample was cut into cuboid shapes with the following dimensions: length, 10 mm; width, 5 mm; and thickness, 2 mm. Each group of samples was measured thrice, and the data were collated and analysed. Next, we soaked 25 CEF/Fe$_3$O$_4$/HA/CS/PQQ layered scaffolds (5 mm in diameter and 2 mm in thickness) in 5 mL of phosphate-buffered saline (PBS). We extracted 1 mL of the PBS at different time points and added an equal volume of PBS to maintain a constant total volume. The extracted liquids were subjected to high-performance liquid chromatography (HPLC, Agilent, USA) at different time points to detect the concentration of the drug released.

2.7. Assessment of cell viability and adhesion

The culture medium used to grow MC3T3-E1 cells was 10% FBS), 1% penicillin-streptomycin, and osteogenic induction medium. Every 100 mL of the osteogenic induction medium contained 10 μL of dexamethasone (1 mM), 500 μL of vitamin C (1 mM), and 1 mL of β-glycerophosphate (1 M). Bone marrow macrophages (BMMs) were collected from the tibias and femurs of 4-6-week-old C57BL/6 mice and incubated in α-MEM containing 30 ng/mL M-CSF, 10% FBS, and 1% penicillin-streptomycin. The viability experiment was performed using the extraction liquid method of the CS, CEF/Fe$_3$O$_4$/HA/CS, and CEF/Fe$_3$O$_4$/HA/CS/PQQ layered scaffolds. Briefly, MC3T3-E1 cells were assayed for viability using a Cell Counting Kit 8 (CCK-8; Dojindo, Kumamoto, Japan) according to the manufacturer's instructions. To evaluate cell adhesion on the scaffold, we co-cultured MC3T3-E1 cells with the scaffold for 24 h, removed the spent medium, washed the cells twice with PBS, and fixed them with 4% paraformaldehyde. The samples were then graded, dehydrated, and freeze-dried. Finally, SEM (Sirion 200, FEI, Hillsboro, OR, USA) was used to characterise the morphology of the cells on the scaffolds. The extracts were prepared according to the ISO 10993–5. The ratio of mass to extraction medium was 0.2 g/mL, and the immersed samples were kept in a humidified atmosphere with 5% CO2 at 37 C for 24 h [33].

2.8. Alkaline phosphatase (ALP) staining and alizarin red (AR) staining

MC3T3-E1 cells were seeded at a density of 5 × 10^5 cells per well in 6-well plates for 24 h. The spent cell culture medium was then changed to a liquid containing CS, CEF/Fe$_3$O$_4$/HA/CS, and CEF/Fe$_3$O$_4$/HA/CS/PQQ layered scaffolds soaked in osteogenic induction medium. The medium was changed every two days. For the ALP staining experiments, we cultured the above samples for seven days and then terminated the culture. The cultures were then fixed in 4% paraformaldehyde and washed three times with PBS. An ALP staining kit (Hongqiao, Shanghai, China) was then used according to the manufacturer's instructions.

For the AR staining experiments, the samples were incubated for 21 days, and the incubation conditions were the same as above. An AR staining kit (Sigma-Aldrich, Darmstadt, Germany) was used according to the manufacturer's instructions. Finally, the samples were observed under an optical microscope.

2.9. Migration and tube formation assay

Here, 8-μm pore size Transwell plates (No. 3422; Corning, NY, USA) were used for cell migration experiments and were placed in 24-well plates. Human umbilical vein endothelial cells (HUVECs) were seeded in the upper chamber of the Transwell at a density of 5.0 × 10^4. The extracted CS, CEF/Fe$_3$O$_4$/HA/CS, and CEF/Fe$_3$O$_4$/HA/CS/PQQ layered scaffolds were placed in the lower chamber. The samples were then incubated for 24 h. Next, we removed the Transwell plate and wiped the cells on the membrane with a cotton swab. The cells were then fixed with 4% paraformaldehyde for 10 min and then washed three times with 0.5% crystal violet staining. For the cell tube formation experiments, 15-well μ-Slides (ibidi, Germany) were seeded with 10 μL Matrigel (BD Biosciences, Franklin Lakes, NJ, USA) and placed in a cell incubator for 30 min. HUVECs were seeded on the Matrigel at a density of 10^4. After 6 h of incubation, the number of intact junctional loops formed by the cells was counted to assess tubule-forming capacity. The samples were observed under an optical microscope.

2.10. Tartrate-resistant acid phosphatase staining (TRAP) and F-actin

The medium used to culture bone marrow macrophages (BMMs) were the extracts of each scaffold group, containing 30 ng/mL M-CSF, 50 ng/mL RANKL, and 10% FBS. The medium was replaced every two days. After seven days, the samples were stained according to the instructions of a TRAP staining kit (Sigma-Aldrich, Darmstadt, Germany). Finally, the samples were observed under an optical microscope. Cells with more than three nuclei were considered positive for TRAP.

For the F-actin staining experiments, samples were incubated with rhodamine-conjugated phalloidin (Cytoskeleton Inc., Denver, CO, USA) for 15 min, washed three times with PBS, stained with DAPI for 5 min, and washed thrice with PBS. The cytoskeleton was visualised using an LSM5 confocal microscope (Carl Zeiss AG, Oberkochen, Germany). The total area of the osteoclasts and the number of nuclei were quantified using ImagePro Plus 6.0 software (Media Cybernetics, Inc., Rockville, MD, USA).

2.11. RT-PCR and western blot

Osteoblasts and osteoclasts were cultured as described above. After 7 days of incubation, the cultures were terminated. Total RNA was extracted using an RNeasy Mini Kit (Qiagen, Inc., Valencia, CA, USA) according to the manufacturer's instructions. First-strand cDNA was reverse-transcribed from the isolated RNA using a Takara kit. A SYBR Premix Ex Taq kit (Takara Biotechnology Co., Ltd.) and ABI 7500 Sequencing Detection System (Applied Biosystems; Thermo Fisher Scientific, Inc.) were used to perform qPCR. All reactions were performed in triplicate. GAPDH was used as the reference gene. The PCR primers used to amplify the target genes were shown in Table 1.

In addition, the expression of osteoblast-related proteins (COL1, ALP, Runx-2, and OPG) and osteoclast-related proteins (NFATc1, c-Fos, p-NFκB-p65, and p-IκBα) were also detected. The cell culture conditions were the same as those previously described. First, we added 200 μL radioimmunoprecipitation assay (RIPA) lysis buffer containing 1 μM protease inhibitor into each well of a 6-well plate and lysed the cells for 10 min. The samples were then collected and centrifuged at 12,000×g for 10 min to remove the pellets. A bicinchoninic acid (BCA) assay was used to measure the total protein concentration. Briefly, a protein loading buffer was added to the sample. The samples were then placed in a high-temperature container at 95 °C for 15 min to denature the proteins.

Table 1
PCR primers were designed to amplify the genes of interest are shown below.

COL-1- forward	5′- GAGAGGTGAACAAGGTCCCG -3′
COL-1-reverse	5′- AAACCTCTCTCGCCTCTTGC -3′
BMP-2- forward	5′- GGAACGGACATTCGGTCCTT -3′
BMP-2-reverse	5′- CACCATGGTCGACCTTTAGGA -3′
RUNX-2- forward	5′- TCGGAGAGGTACCAGATGGG-3′
RUNX-2-reverse	5′- TGAAACTCTTGCCTCGTCCG-3′
C-fos- forward	5′- AGAAACACGTCTTCCCTCGA -3′
C-fos-reverse	5′- TTGCCAGGAACACAGTAGGT -3′
NFATc1- forward	5′- CAACGCCCTGACCACCGATAG-3′
NFATc1-reverse	5′- GGCTGCCTTCCGTCTCATAGT-3′
GAPDH- forward	5′- CACCACCATGGAGAAGGCCG-3′
GAPDH -reverse	5′- ATGATGTTCTGGGCAGCCCC-3′

Finally, the proteins were separated via electrophoresis, and the proteins were transferred onto a membrane. The membranes were blocked with a milk solution and were then incubated with the primary antibodies at 37 °C overnight. Antibodies against NFATc1 (abs135966, absin), c-FOS (abs155908, absin), p-NFκB-p65 (GB11142-1, Servicebio), and p-IκBα (GB13462, Servicebio) were purchased from absin and Servicebio, respectively. Then, the membranes were incubated with the corresponding diluted horseradish peroxidase (HRP)-conjugated secondary antibodies (1:1000) for 1 h at 37 °C in the dark and washed thrice with TBST for 10 min each time. Finally, the membranes were exposed using an Amersham Imager 680 instrument (GE Healthcare Life Sciences). The grey values of the bands were measured and analysed using ImageJ software.

2.12. Establishment of an animal model and micro-CT analysis

The experimental design required 15 female Sprague-Dawley (SD) rats (6-week-old, weight $= 200 \pm 15$ g, n $= 5$ rats per group). A pore size defect with a diameter of 5 mm and a height of 2 mm in the bilateral calvaria was used to evaluate bone regeneration in a rat model. The method was the same as previously described. The bone defects were filled with the three treatments: CS, CEF/Fe$_3$O$_4$/HA/CS, and CEF/Fe$_3$O$_4$/HA/CS/PQQ layered scaffolds. Briefly, the periosteums of the rats were removed, and their skin was sutured. The purpose of removing the periosteum was to verify endochondral osteogenesis rather than subperiosteal osteogenesis within the scaffold. After rearing for 12 weeks, the rats were euthanised. The rats were then intraperitoneally injected with fluorescently labelled alizarin red (30 mg/kg; Sigma-Aldrich) and calcein (30 mg/kg; Sigma-Aldrich) at different time points. After rearing for 12 weeks, the rats were euthanised. The skulls of the rats were removed and fixed in 4% paraformaldehyde. Then, the bone defects at the top of the skull were removed and studied using a micro-CT system (Skyscan 1076). The scanning data were then analysed using Skyscan CTAn software.

2.13. Fluorescent double labeling, H&E, immunofluorescence and immuno-histochemistry

The samples were then dehydrated in ethanol and embedded in poly (methyl methacrylate). Thin sections of 100-μm thickness were cut using a hard tissue microtome (SP1600, Leica, Germany) and polished to a final thickness of 40 μm. Finally, the sections were observed under a confocal microscope (Alizarin red: 543/580–670 nm; calcein: 488/500–550 nm) to evaluate new bone tissue. To observe bone and collagen regeneration, the above samples were embedded with gradient dehydration staining, sectioned, stained with H&E, and observed under a light microscope. The samples were then incubated overnight with primary antibodies (CD31, OPG, RANKL, IL-1β, TNF-α, BMP-2, RUNX-2, and OPN). The antibodies against CD31 (GB113151), OPG (GB11151), RANKL (GB11235), TNF-α (GB13452), IL-1β, BMP-2 (GB11252), RUNX-2 and OPN were purchased from Servicebio company (Wuhan, China). When conducting immunofluorescence experiments, we chose secondary antibodies of different colours (pink for CD31, green for OPG, and red for RANKL) and incubated them with the cells in the dark for 1 h. Finally, all the above samples were scanned on the machine.

2.14. statistical analysis

All results were presented as the mean $\pm$ standard deviation (SD). Comparisons between groups were performed using one-way analysis of variance (ANOVA). Statistical analyses were performed using GraphPad Prism 6 software (CA, USA). Statistical significance was set at **$P < 0.01$ and *$P < 0.05$.

3. Result

3.1. Microstructures of CEF, CEF/Fe₃O₄, CEF/Fe₃O₄/HA

In this study, CEF was loaded with a layer of nano-ferric oxide, and then a layer of hydroxyapatite was deposited on its surface via chemical co-precipitation to make it both magnetic and applicable for bone repair. The surface morphology of the CEF was analysed via SEM. As shown in Fig. 1a and (b), the surface of the CEF was smooth and regular, with a diameter of approximately 20 μm. As shown in Fig. 1d and (e), CEF/Fe$_3$O$_4$ composite fibres loaded with Fe$_3$O$_4$ had a rough surface. Fig. 1g and (h) show the SEM images of the CEF/Fe$_3$O$_4$/HA surface topography, where granular HA blocks were deposited on the surface of the material. Fig. 1c, f, i show the uniform distribution of Ca, P, and Fe on the fibre surface, while EDS (Fig. 1j) further proved that the surface of the cellulose fibre was successfully formed from Fe$_3$O$_4$ and HA layers.

3.2. Characterization of CEF/Fe₃O₄/HA/CS scaffold

Cellulose fibre-reinforced hydroxyapatite/chitosan scaffolds with a magnetic orientation were prepared via freeze-drying under a magnetic field. Through SEM analysis, it was observed that the surface morphology of the CEF/Fe$_3$O$_4$/HA/CS scaffold on the fracture surface was a regular layered structure (Fig. 2a and b), and the gap between layers was 100–200 μm. A gap this wide can provide ample space for cell growth, proliferation, and migration. Fig. 2c shows an SEM image of the cross-section of the CEF/Fe$_3$O$_4$/HA/CS scaffold. It can be observed that the fibres were aligned in the cross-section of the scaffold. Fig. 2d, e shows an SEM image of the fracture surface of the CEF/Fe$_3$O$_4$/HA/CS/PQQ scaffold. Compared with Fig. 2a and (b), there is no significant difference, and it is also a layered structure with a gap width of approximately 200 μm. This suggests that the introduction of drugs did not affect the scaffold structure. Fig. 2f shows an SEM image of the cross-section of the CEF/Fe$_3$O$_4$/HA/CS/PQQ scaffold. Similarly, compared with Fig. 2c, there was no significant difference, and the arrangement of the fibres is obvious. Fig. 2g, h, i, j, k represents the distribution images of C, N, O, Ca, P, and Fe in the CEF/Fe$_3$O$_4$/HA/CS scaffold, indicating the scaffold material is composed of these elements. Fig. 2l shows an EDS image of the CEF/Fe$_3$O$_4$/HA/CS scaffold, which further proves that the scaffold material is composed of the above elements without any other redundant peaks, indicating that the prepared scaffold is relatively pure. The chemical formula of PQQ was $C_{14}H_6N_2O_8$, and its main component elements were C, N, and O. There are no special elements, and their contents are very low, so there is no remarkable difference in the SEM and EDS images.

The phase composition and functional groups present in the scaffolds were analysed using XRD and FTIR spectra, respectively. Fig. 3a shows the XRD patterns of the CS, CEF/Fe$_3$O$_4$/HA/CS, and CEF/Fe$_3$O$_4$/HA/CS/PQ scaffolds. Because chitosan (CS) is a semi-crystalline material, there is only one wide peak, its characteristic peak at $2\theta = 20°$. In the CEF/Fe$_3$O$_4$/HA/CS scaffolds, in addition to the wide peak of chitosan, the characteristic diffraction peaks of Fe$_3$O$_4$ and hydroxyapatite (HA) were also observed. The main peaks of Fe$_3$O$_4$ at (220), (311), and (400) and the main characteristic diffraction peaks of HA at 25.8 (002), 28.9 (210), 31.7 (211), 32.8 (300), and 34.0 (202) were consistent with their
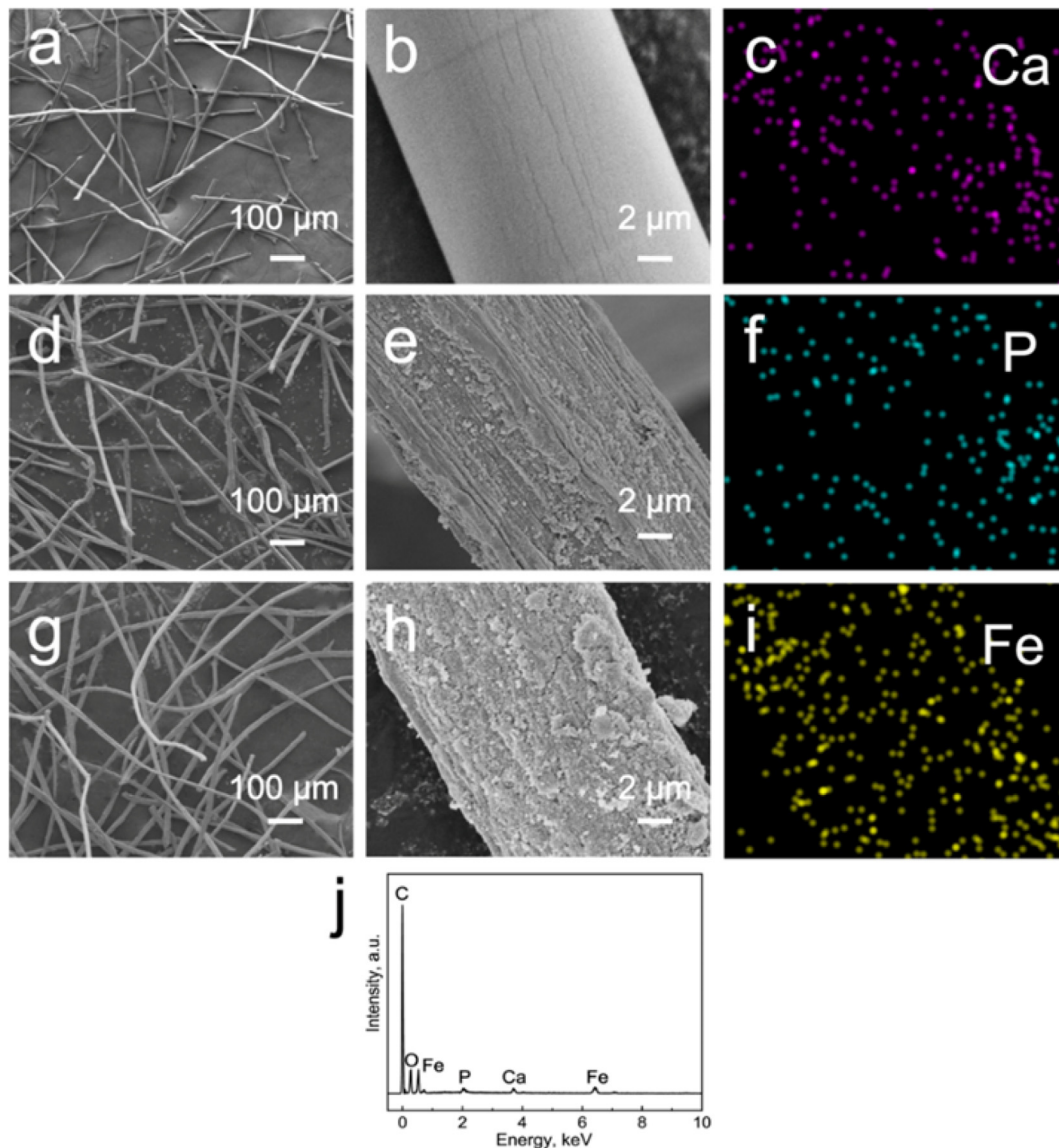
Fig. 1. SEM images, EDS pattern, Distribution map of different materials: (a, b) SEM images of CEF; (d, e) SEM images of CEF/Fe$_3$O$_4$; (g, h) SEM images of CEF/Fe$_3$O$_4$/HA; (c, f, i) Ca, P, Fe elements distribution map of CEF/Fe$_3$O$_4$/HA; (j) EDS spectra of CEF/Fe3O4/HA.

respective standard PDF cards. These peaks were due to the attachment of Fe$_3$O$_4$ and HA to the cellulose fibres. However, the characteristic XRD peaks of the CEF/Fe$_3$O$_4$/HA/CS/PQQ scaffolds were the same as those of the CEF/Fe$_3$O$_4$/HA/CS scaffold. A possible reason for this is that PQQ is an amorphous material and its proportion in the scaffold is minimal, thereby showing no new characteristic diffraction peaks.

Fig. 3b shows the FTIR spectra of the three types of scaffolds. The shapes of the FTIR spectra of the three kinds of scaffolds were similar, mainly showing the infrared absorption peak of CS. The infrared absorption peak at 3454 cm^{-1} is formed by the stretching vibration absorption peak of the hydroxyl group (-OH) and the stretching vibration absorption peak of –NH in chitosan. A strong amide I absorption peak near 1640 cm^{-1} was also observed. The infrared absorption peak at approximately 1597 cm^{-1} corresponds to amide II, while the infrared absorption peak at 1420 cm^{-1} corresponds to = CH$_2$ bending and –CH$_3$ deformation. The infrared absorption peak observed at 1378 cm^{-1} is associated with C–H bending and –CH$_3$ symmetric deformation vibration. The absorption peaks at 898–899 cm^{-1} correspond to the C–O stretching vibration. The infrared spectra of the scaffold materials with three different components are the same, which may be due to the large content of CS and the large number of functional groups in CS. Hence, the

introduction of CEF and the drug PQQ did not show any new infrared absorption peaks.

To study the effect of introducing oriented fibres on the mechanical properties of scaffolds, the tensile and compressive properties of the scaffolds perpendicular to the fibre direction, parallel to the fibre direction, and without fibres were tested. A universal electronic testing machine was used to conduct tensile and compression tests on the composite material to determine the total force it could withstand. Each group was tested thrice in parallel. Fig. 4a, b, c shows the tensile performance curves of the scaffold perpendicular to the fibre direction, parallel to the fibre direction, and in the fibre-free direction, respectively. As shown in Fig. 4a, the tensile strength of the scaffolds perpendicular to the fibre direction was measured thrice, and the results were 6.4, 6.7, and 6.5 Mpa, with an average maximum tensile strength of 6.53 MPa. In Fig. 4b, the tensile strength of the scaffold in the direction parallel to the fibres were 3.2, 3.5, and 3.4 Mpa, with an average maximum tensile strength of 3.36 MPa. In Fig. 4c, the tensile strength of the fibre-free scaffold was measured to be 1.7, 1.6, and 1.7 MPa, with an average maximum tensile strength of 1.67 MPa. Hence, it can be concluded that the maximum tensile strength of the scaffolds with oriented fibres was anisotropic along different fibre directions. The maximum tensile strength was found
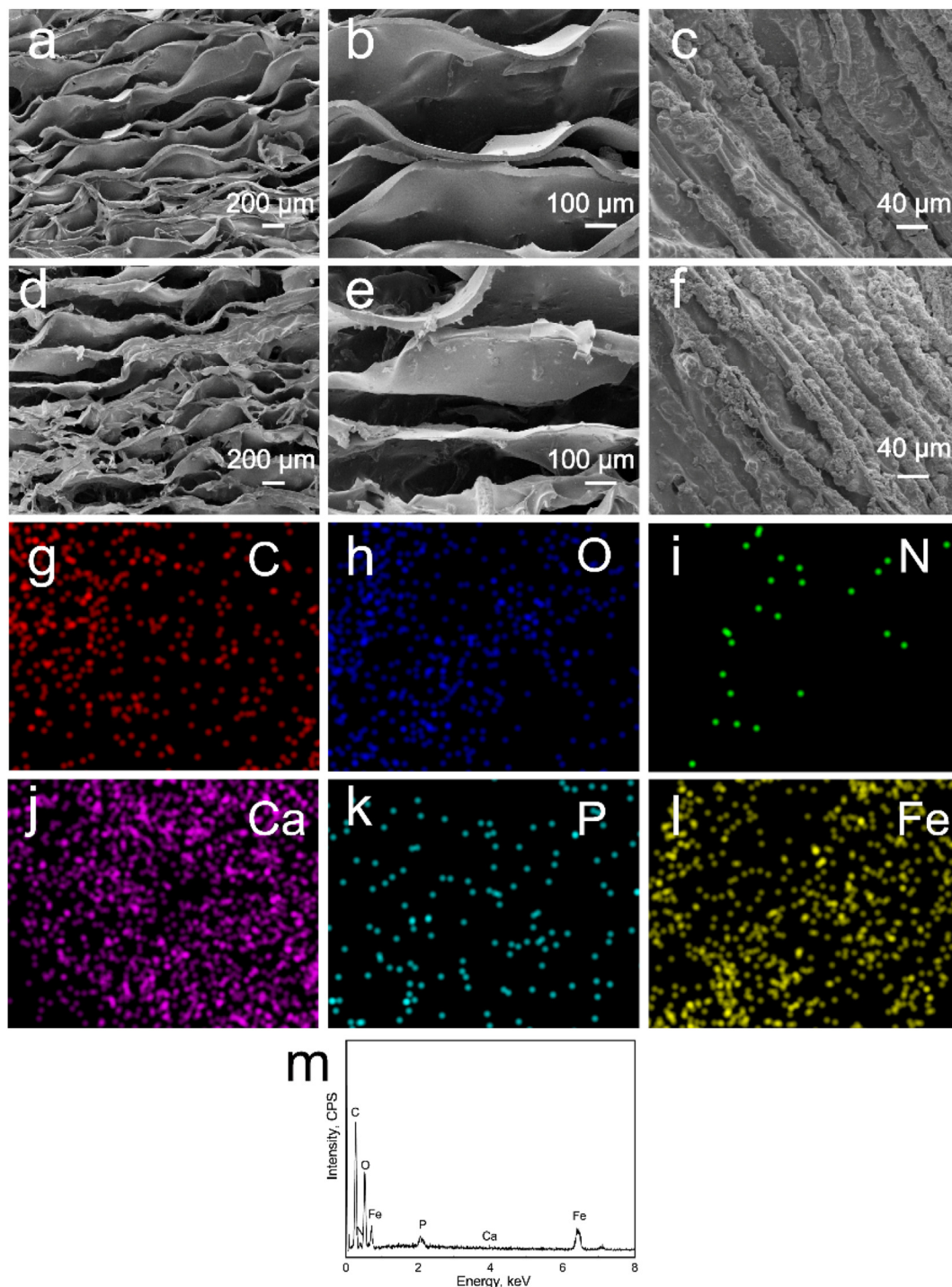
Fig. 2. (a, b) fracture surface and (c) cross section SEM images of CEF/Fe₃O₄/HA/CS scaffold; (d, e) fracture surface and (f) cross section SEM images of CEF/Fe₃O₄/HA/CS/PQQ scaffold; (g, h, i, j, k, l) Surface scan map of C, O, N, Ca, P, Fe elements from CEF/Fe₃O₄/HA/CS scaffold; (m) EDS spectra of CEF/Fe3O4/HA/CS scaffold.

perpendicular to the fibre direction, followed by the tensile strength parallel to the fibre direction, while the tensile strength of the scaffold without fibres was the lowest. The above results indicate that the introduction of fibres enhanced the tensile strength of the scaffold material since the tensile strength perpendicular to the fibre direction increased by approximately 289% compared to that without fibres. These differences were statistically significant.

To further test the mechanical properties of the scaffold material, we tested the compression properties of the scaffold material along different directions of the fibre. Fig. 4d, e, f shows the compression performance curves of the scaffold in the vertical fibre, parallel fibre, and non-fibre directions, respectively. In Fig. 4d, the compressive strength of the bracket in the vertical fibre direction was 1.7, 1.6, and 1.6 MPa respectively, with an average maximum compressive strength of 1.63 MPa. In Fig. 4e, the compressive strength of the bracket in the parallel fiber direction yielded 0.9, 1.0, and 1.1 MPa, with an average maximum compressive strength of 1.0 MPa. In Fig. 4f, the compressive strength of the fibreless scaffold was determined as 0.5, 0.5, and 0.4 Mpa, with an average maximum compressive strength of 0.47 MPa. Similar to the tensile strength results mentioned above, the introduction of oriented
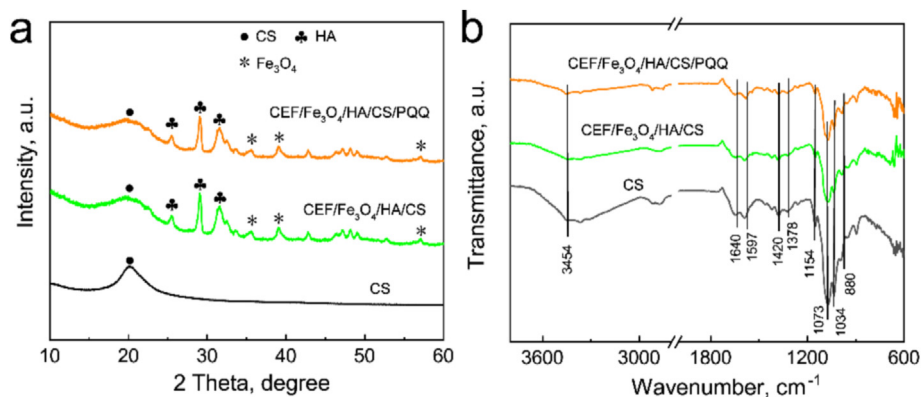
Fig. 3. (a) XRD patterns of CS, CEF/Fe₃O₄/HA/CS and CEF/Fe₃O₄/HA/CS/PQQ scaffold; (b) FTIR patterns of CS, CEF/Fe₃O₄/HA/CS and CEF/Fe₃O₄/HA/CS/PQQ scaffold.
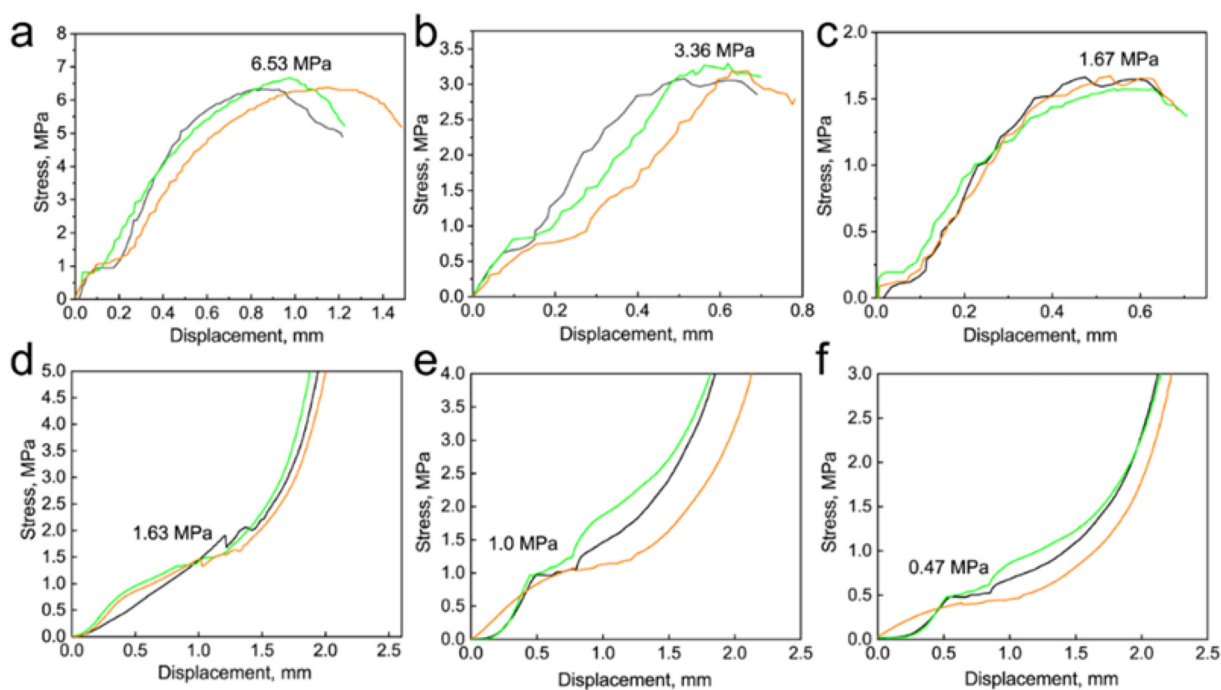

Fig. 4. The tensile curves and compression curves of different scaffolds: (a) the tensile curve of stretch the scaffold perpendicular to the fiber direction; (b) the tensile curve of stretch the scaffold parallel to the fiber direction; (c) the tensile curve of scaffolds without fibers; (d) the compression curve of vertical fiber directional compression scaffold; (e) the compression curve of parallel fiber directional compression scaffold; (f) the compression curve of scaffold without fibers.

fibres enhanced the compressive properties of the scaffolds, and the maximum compressive strength was anisotropic along the different directions of the fibres. The compression performance was the highest in the vertical (perpendicular) direction and the lowest in the absence of fibres.

We also tested the swelling and degradation properties of scaffolds with different components. We found that the introduction of oriented fibres and the drug PQQ did not affect the swelling and degradation capacity of the scaffolds; it even imparted good swelling properties and a slow degradation rate. Fig. 5a shows the time-course swelling properties of the CS, CEF/Fe₃O₄/HA/CS, and CEF/Fe₃O₄/HA/CS/PQQ scaffolds within 24 h. It can be seen from the figure that the three curves showed similar trends. In the first 6 h, the scaffold absorbed water rapidly and expanded, reaching equilibrium in 12 h, indicating that the scaffold reached the saturation state of water absorption. Compared with the initial mass, the maximum mass ratio of the scaffold after water absorption was increased approximately eight-fold, indicating that the scaffold had excellent water absorption capacity and ensured good

biocompatibility. The curves in Fig. 5b represent the time-course mass loss curves for the CS, CEF/Fe₃O₄/HA/CS, and CEF/Fe₃O₄/HA/CS/PQQ scaffolds within 14 days. The degradation curves of the three different scaffolds showed similar trends, indicating that the introduction of oriented fibres and the drug PQQ did not affect the degradation of the scaffolds. As shown in the figure, after soaking in PBS for 14 days, the mass loss of the three scaffolds was only approximately 16%, indicating that the scaffolds degraded slowly. This demonstrated the continuous drug delivery performance of the scaffold and the continuous provision of essential elements for bone repair, further indicating that the scaffold is a good bone repair material.

In addition, to simulate the drug release performance of the scaffold *in vivo*, we conducted *in vitro* experiments. Twenty-five samples of CEF/Fe₃O₄/HA/CS/PQQ scaffolds with a diameter of 5 mm and a thickness of 2 mm were soaked in 5 mL PBS. At predetermined time points, 1 mL of the PBS solution was extracted, and 1 mL fresh PBS was added to maintain a constant medium volume. The concentration of PQQ released was determined via HPLC (Agilent 1100, USA). All drug release tests
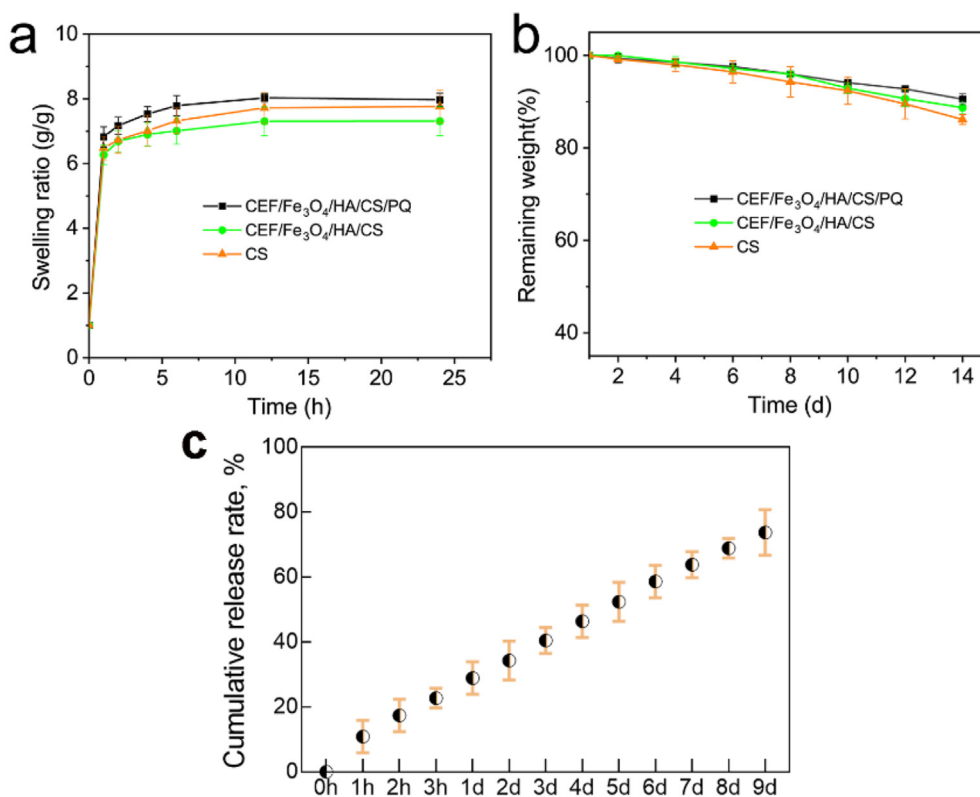
Fig. 5. Swelling and degradation of CS, CEF/Fe$_3$O$_4$/HA/CS and CEF/Fe$_3$O$_4$/HA/CS/PQQ scaffolds: (a) swelling curve; (b) degradation curve. (c) Cumulative drug release rate at 72 h of the CEF/Fe$_3$O$_4$/HA/CS/PQQ stent.

were repeated three times under the same conditions. As shown in Fig. 5c, the drug-loaded scaffold released PQQ rapidly in the first 24 h, slowed down until 48 h. The above results indicated that the scaffold was a good drug carrier with a sustained-release capability.

3.3. The CEF/Fe$_3$O$_4$/HA/CS/PQQ scaffold promotes osteoblast differentiation in vitro

Fig. 6a shows the effects of the CS, CEF/Fe$_3$O$_4$/HA/CS, and CEF/Fe$_3$O$_4$/HA/CS/PQQ scaffolds on the proliferation of MC3T3-E1 cells. We found that the CEF/Fe$_3$O$_4$/HA/CS/PQQ scaffolds slightly promoted cell proliferation but were not toxic to MC3T3-E1 cells. SEM imaging showed that bone marrow mesenchymal stem cells showed good adhesion to the surfaces of the different scaffolds (Fig. 6d). We observed pseudopod extensions on the surface of the oriented cellulose fibres in the scaffold, which further indicated that the scaffold had good biocompatibility with bone marrow mesenchymal stem cells and accelerated their cell adhesion. Next, we verified the effect of the scaffold on osteoblast differentiation. ALP staining (Fig. 6b, e) revealed that the CEF/Fe$_3$O$_4$/HA/CS and CEF/Fe$_3$O$_4$/HA/CS/PQQ scaffolds had a significant effect compared with CS scaffolds. Similar results were observed with AR staining, where a significantly increased number of calcium nodules was observed in the CEF/Fe$_3$O$_4$/HA/CS and CEF/Fe$_3$O$_4$/HA/CS/PQQ scaffolds (Fig. 6c, f)

To further validate the effects of CS, CEF/Fe$_3$O$_4$/HA/CS, and CEF/Fe$_3$O$_4$/HA/CS/PQQ scaffolds on osteoblast differentiation-related genes (*RUNX-2*, *BMP-2*, and collagen 1) and proteins (ALP, RUNX-2, collagen 1, and OPG), we performed RT-PCR (Fig. 6g, h, i) and western blotting (Fig. 6j). Fig. 6g, (h), and (i) show that the gene expressions of *RUNX-2*, *BMP-2*, and *Collagen 1* were upregulated in cells grown in CEF/Fe$_3$O$_4$/HA/CS/PQQ scaffolds compared to those grown in CEF/Fe$_3$O$_4$/HA/CS scaffolds and CS scaffolds. ALP, a specific marker of osteoblast maturation, is an enzyme secreted by osteoblasts. Fig. 6k shows that ALP expression in cells grown on CEF/Fe$_3$O$_4$/HA/CS and CEF/Fe$_3$O$_4$/HA/CS/

PQQ scaffolds was higher than that of those grown on CS scaffolds. This result was similar to that shown in Fig. 6b. RUNX-2 is a transcription factor that regulates the differentiation of mesenchymal stem cells into osteoblasts and regulates the expression of Collagen 1, which is essential in endochondral osteogenesis. OPG is also expressed in osteoblasts and is specific to osteoblast differentiation. OPG and RANKL are the key proteins that regulate osteoclast differentiation.

3.4. The CEF/Fe$_3$O$_4$/HA/CS/PQQ scaffold inhibits osteoclast differentiation in vitro

Another purpose of using the fabricated scaffolds was to solve the imbalance in bone homeostasis mediated by acute inflammatory responses. Hence, we deposited nano-hydroxyapatite particles on the surface of the cellulose fibres, which imitated the cell matrix of the human bone tissue. On the other hand, the gaps between the nano-hydroxyapatite particles served as vessels for carrying drugs. We loaded the drug PQQ, which inhibits the NF-κB signalling pathway, on the surface of nano-hydroxyapatite.

Fig. 7a, (b), (c), and (d) show the results of the TRAP and F-actin staining. The above figures show that the number of TRAP-positive cells (Fig. 7e) and the area of osteoclasts (Fig. 7f) in the CEF/Fe$_3$O$_4$/HA/CS group and the CEF/Fe$_3$O$_4$/HA/CS/PQQ group were reduced. The inhibitory effect of the scaffolds against osteoclasts was most obvious in the CEF/Fe$_3$O$_4$/HA/CS/PQQ group. Similar results were obtained in the F-actin staining assay. The results show that, compared with the CS group, the CEF/Fe$_3$O$_4$/HA/CS group and the CEF/Fe$_3$O$_4$/HA/CS/PQQ group inhibited osteoclast F-actin expression more significantly (Fig. 7g). To further verify the expression of key genes related to osteoclast differentiation (c-Fos, and NFATc1), we performed RT-PCR (Fig. 7h and i). The results showed that the expression of osteoclast-specific genes was significantly downregulated in the CEF/Fe$_3$O$_4$/HA/CS group and the CEF/Fe$_3$O$_4$/HA/CS/PQQ group compared with the CS group. Moreover,
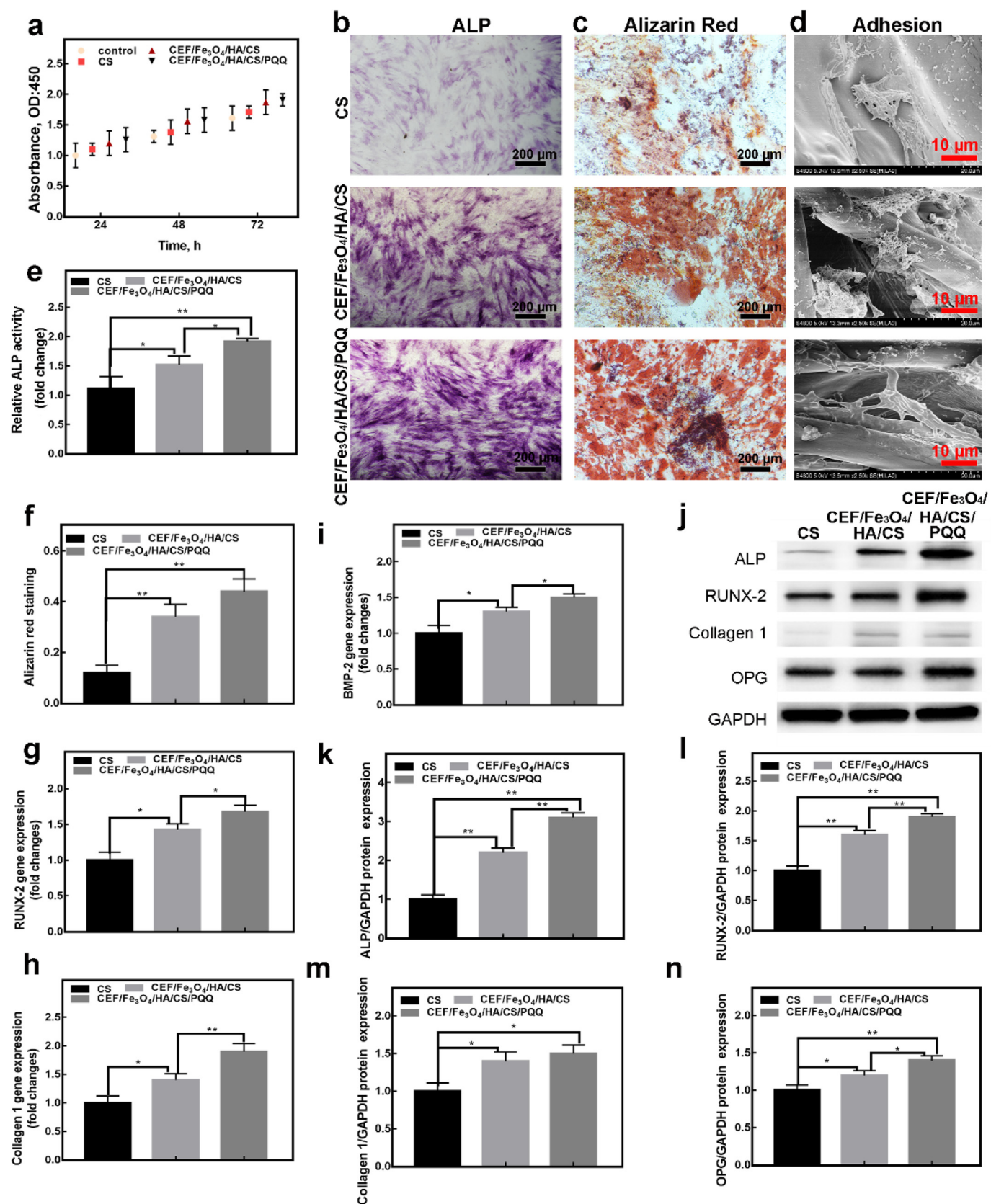
Fig. 6. The effect CS, CEF/Fe$_3$O$_4$/HA/CS and CEF/Fe$_3$O$_4$/HA/CS/PQQ scaffolds on the differentiation of osteoblasts. (a) CCK-8; (b, c) ALP staining and AR staining; (d) adhesion; (e, f) Statistical analysis of ALP staining and AR staining; (g, h, i) RUNX-2 gene, Collagen1 gene and BMP-2 gene expression; (j) Western blot; (k, l, m, n) Statistical analysis of ALP, RUNX-2, Collagen1 and OPG.
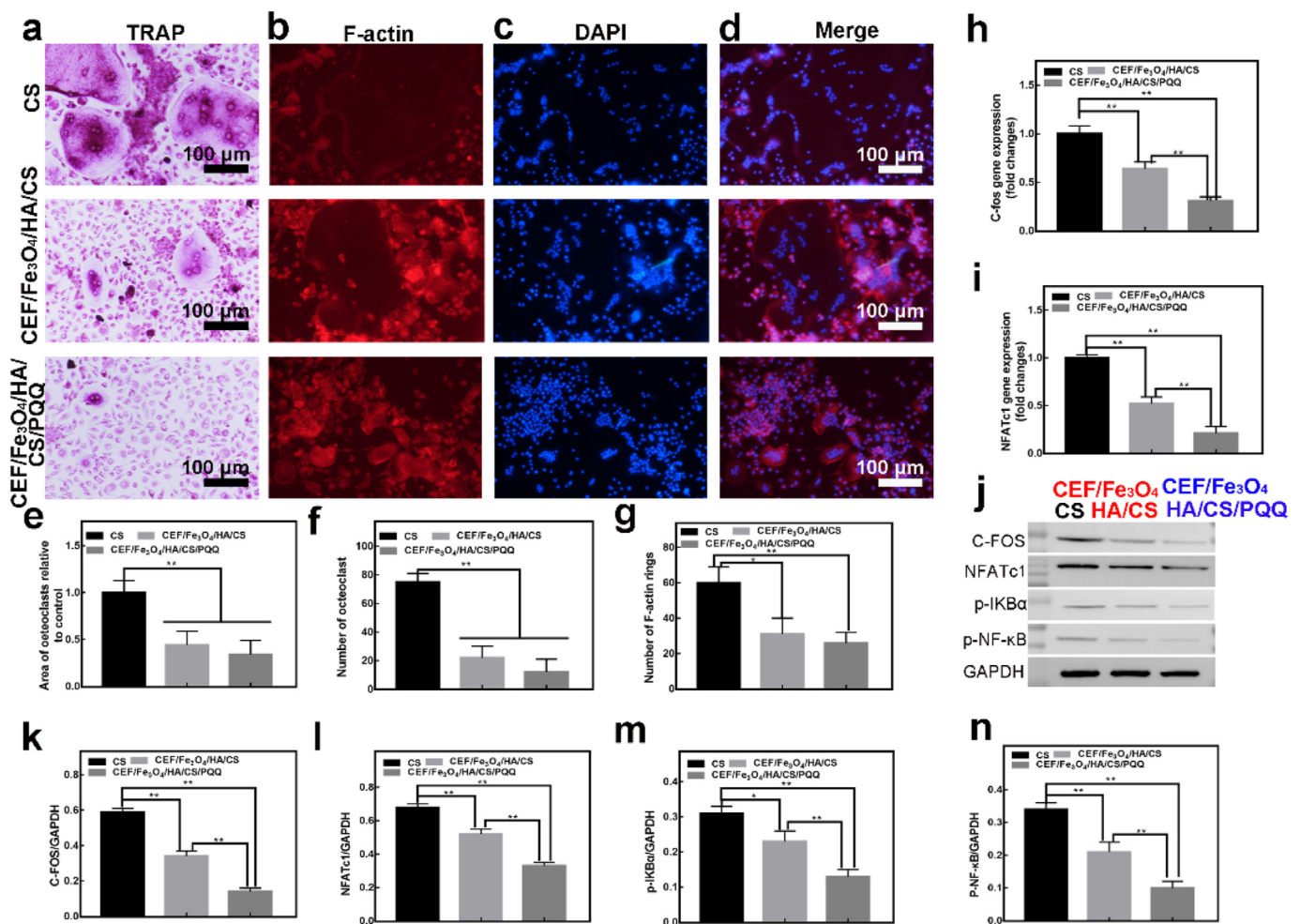
Fig. 7. The effect CS, CEF/Fe$_3$O$_4$/HA/CS and CEF/Fe$_3$O$_4$/HA/CS/PQQ scaffolds on the differentiation of osteoclasts. (a) TRAP staining; (b, c, d) F-actin, DAPI and Merge of osteoclasts; (e, f, g) Statistical analysis of osteoclast area, number of positive cells and number of F-actin rings; (h, i) Expression of osteoclast differentiation-related genes (Nfatc1 and C-fos); (j) Expression of osteoclast differentiation-related proteins (C-FOS, NFATc1, p-IKBα and p–NF–κB); (k, l, m, n) Statistical analysis of the above proteins.

this inhibitory effect was more pronounced after adding PQQ to the CEF/Fe$_3$O$_4$/HA/CS scaffolds, since PQQ inhibits the NFκB pathway, subsequently inhibiting osteoclast differentiation. We performed further validation at the protein level, and the results were similar to those obtained via RT-PCR (Fig. 7k and l). Fig. 7j, (m), and (n) show that IκBα and NFκB were activated in the CS group, while IκBα and NFκB were inhibited in CEF/Fe$_3$O$_4$/HA/CS group, and the CEF/Fe$_3$O$_4$/HA/CS/PQQ group. After adding PQQ, the inhibition effect was more obvious.

3.5. The CEF/Fe$_3$O$_4$/HA/CS/PQQ scaffold promotes angiogenesis in vitro

When designing the CEF/Fe$_3$O$_4$/HA/CS/PQQ scaffold, we imitated the arrangement and structure of the collagen fibres and hydroxyapatite components of the extracellular matrix in the bone tissue. In addition, there are longitudinally arranged blood vessels in normal bone tissue that provide nutrients to osteoblasts. Considering that the collagen fibres formed inside the layered CEF/Fe$_3$O$_4$/HA/CS/PQQ scaffold are mineralised into bone tissue, the ingrowth of new blood vessels must occur.

To investigate the effect of the CS, CEF/Fe$_3$O$_4$/HA/CS, and CEF/Fe$_3$O$_4$/HA/CS/PQQ scaffolds on vascular endothelial cell migration, we performed Transwell assays and evaluated their ability for HUVEC recruitment. Crystal violet staining (Fig. 8a) revealed that the migration ability of the cells grown in the CEF/Fe$_3$O$_4$/HA/CS group was much higher than that of the CS group. In addition, the migration ability of the cells improved when PQQ was added to the CEF/Fe$_3$O$_4$/HA/CS scaffold.

Subsequently, a quantitative statistical analysis of the number of cells in the Transwell was performed. These conclusions were similar to those expected (Fig. 8b).

We also performed tube formation experiments on HUVECs, where we observed the formation of a tube-like structure when the cells were cultured in the scaffold extracts. The number of tubes formed in the CEF/Fe$_3$O$_4$/HA/CS and CEF/Fe$_3$O$_4$/HA/CS/PQQ groups was significantly higher than that in the CS group, and the number of tubes in the CEF/Fe$_3$O$_4$/HA/CS/PQQ group was also higher than that in the CEF/Fe$_3$O$_4$/HA/CS group (Fig. 8c and d).

3.6. Osteogenic activities of CEF/Fe$_3$O$_4$/HA/CS/PQQ scaffolds in vivo

Subsequently, a rat skull defect model was constructed. By filling the skull defects with the scaffold and removing the periosteum during the operation, this study focused on the mineralisation of endogenous cartilage and the formation of new blood vessels in the layered CEF/Fe$_3$O$_4$/HA/CS/PQQ scaffold. Fig. 9a shows the μCT images of the rat skulls 12 weeks after the operation. We found that new bone tissue formation in the CEF/Fe$_3$O$_4$/HA/CS group was significantly higher than that in the CS group. When PQQ was added, the bone mass increased further, which was also consistent with the statistical analysis of new bone tissue. We analysed the BV/TV ratio (Fig. 9b) and found that the BV/TV ratio of rats in the CEF/Fe$_3$O$_4$/HA/CS (23.42 ± 3.27%) group and CEF/Fe$_3$O$_4$/HA/CS/PQQ (34.23 ± 2.12%) group were significantly
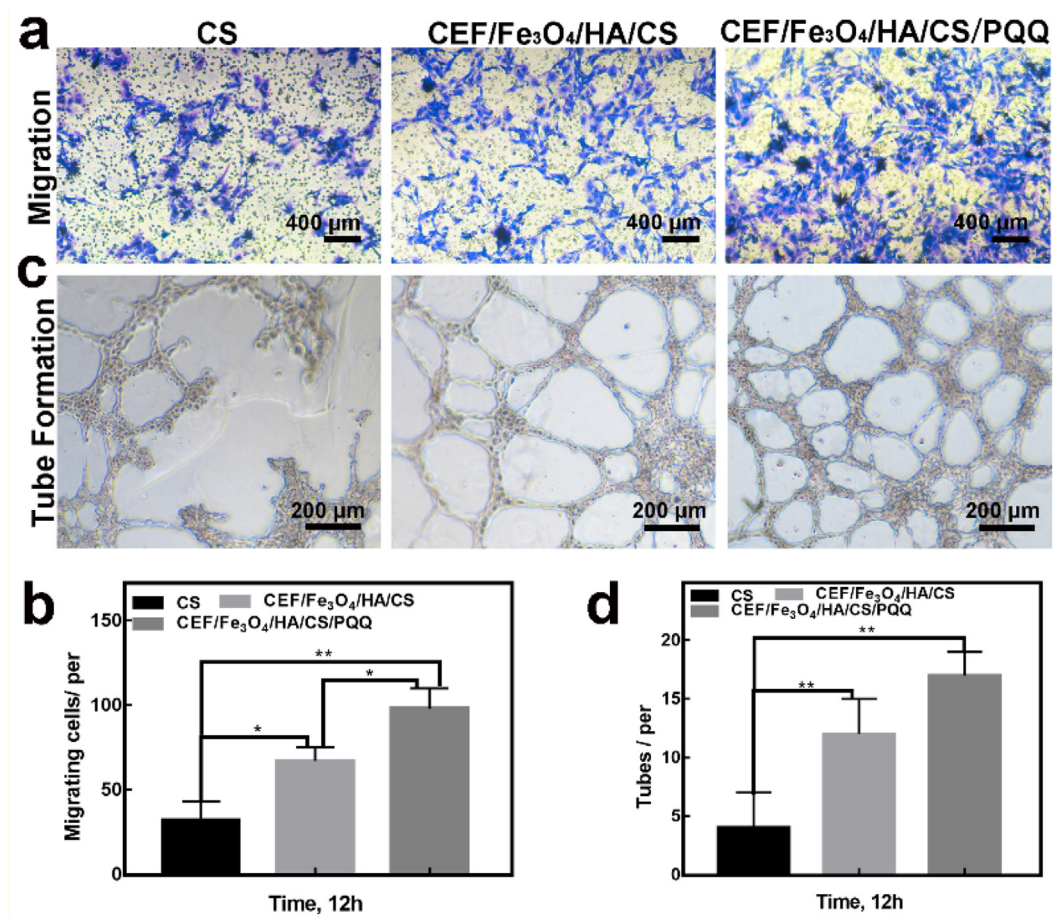
Fig. 8. Effects of different groups on HUVECs. (a) Migration of cells between different groups was assessed by the transwell. (b) Evaluation of tube formation ability of different scaffolds by tube formation experiments. (c, d) Statistical Analysis of (a, c).
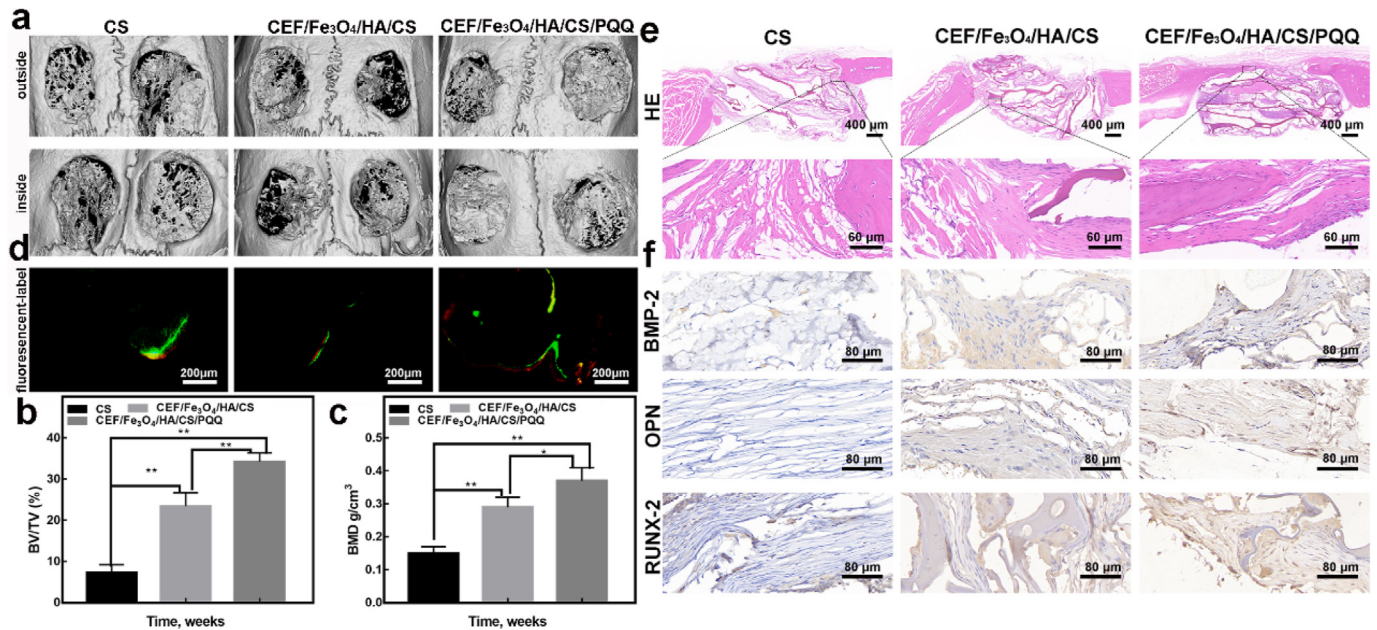

Fig. 9. (a) Micro CT; (b, c) BV/TV ratio and BMD values; (d) serial fluorescent labeling assay; (e) HE; (f) immunohistochemistry for BMP-2, RUNX-2 and OPN.

higher than that of the CS (7.21 ± 2.02%) group. Additionally, the CEF/Fe₃O₄/HA/CS (0.29 ± 0.03 g/cm³) and CEF/Fe₃O₄/HA/CS/PQQ (0.37 ± 0.04 g/cm³) groups had higher BMD values than the CS (0.15 ± 0.02

g/cm³) group (Fig. 9c). Subsequently, bone mineralisation ability was verified using a serial fluorescent labelling assay. The rate of new bone formation in the CEF/Fe₃O₄/HA/CS/PQQ group was 2.9 ± 0.07 μm/d,

while that in the CEF/Fe$_3$O$_4$/HA/CS group was 2.5 $\pm$ 0.09 μm/d. In contrast, the rate of new bone formation in the CS group was only 1.1 $\pm$ 0.11 μm/d (Fig. 9d). Similar results were observed with H&E staining (Fig. 9e). It was also found that new bone tissue formation and collagen I expression were increased significantly in the CEF/Fe$_3$O$_4$/HA/CS/PQQ group and CEF/Fe$_3$O$_4$/HA/CS group. Collagen was filled inside the layered CEF/Fe$_3$O$_4$/HA/CS/PQQ scaffold, and a large amount of nascent extracellular matrix components appeared between the layers, similar to the oriented nano-hydroxyapatite cellulose fibres of the scaffold. The components of the extracellular matrix are mostly collagen fibres and hydroxyapatite. The new collagen tissue was further mineralised to form new bone tissue. BMP-2, RUNX-2, and OPN are important active proteins involved in the formation of new bone tissues. Therefore, we further verified the expression of these osteogenic indicators using immunohistochemistry (Fig. 9f). We found that the protein expression of BMP-2, RUNX-2, and OPN was upregulated in the CEF/Fe$_3$O$_4$/HA/CS/PQQ group, further confirming that these two scaffolds promoted the expression of bone proteins.

Fig. 10 shows the immunohistochemistry (IL-1β and TNF-α) and immunofluorescence (OPG, RANKL, and CD31) staining results. We found that the trend of OPG protein fluorescence intensity was CEF/Fe$_3$O$_4$/HA/CS/PQQ > CEF/Fe$_3$O$_4$/HA/CS > CS. In contrast, the trend in the fluorescence intensity of RANKL protein was the opposite (Fig. 10a and b). The OPG/RANKL ratio is a key factor in regulating bone homeostasis. This may be due to the therapeutic effect of PQQ (an NF-κB pathway inhibitor), which was present in the CEF/Fe$_3$O$_4$/HA/CS/PQQ group. NF-κB pathway inhibitors also inhibit the release of pro-inflammatory factors, such as IL-1β and TNF-α, from macrophages. Pro-inflammatory factors (IL-1β and TNF-α) released by macrophages inhibit angiogenesis. Hence, to investigate this, we used immunofluorescence indicators (such as CD31) to evaluate the formation of new blood vessels (Fig. 10c). We found that the number of new blood vessels in the CEF/Fe$_3$O$_4$/HA/CS/PQQ and CEF/Fe$_3$O$_4$/HA/CS groups was significantly higher than in the CS group. New blood vessels provide a better influx of nutrients for bone tissue. Some studies have shown that the IL-1β and TNF-α released by macrophages inhibit the formation of new bone tissue. Therefore, we performed immunohistochemistry for IL-1β and TNF-α in the above groups (Fig. 10d and e). The results showed that the levels of pro-inflammatory factors in the CEF/Fe$_3$O$_4$/HA/CS/PQQ and CEF/Fe$_3$O$_4$/HA/CS groups were significantly reduced.

4. Discussion

Most of the current degradable bone repair materials imitate the composition of bone, but their mechanical properties are far from those of natural bone [45]. This is largely due to the special structure of natural bones [25,30]. In some studies, the introduction of oriented fibres has been shown to significantly improve the mechanical properties of the scaffold material [25]. In addition, many studies have shown that fibre-oriented scaffolds affect cell growth, morphology, and orientation [23,46]. Here, we focused on the differences in the mechanical properties of scaffolds in different fibre directions and speculated that the mechanical properties of scaffolds would be anisotropic with fibre orientation [47–49]. In previous studies, fibre orientation was found to affect the cell state; therefore, we speculated that fibre-oriented scaffolds might also play a role in promoting osteogenesis and angiogenesis.

Using cellulose fibre and chitosan as raw materials, a magnetically oriented cellulose fibre-reinforced hydroxyapatite/chitosan scaffold was prepared through subjection to a magnetic field and freeze-drying. The magnetic ferric oxide nanoparticles were loaded onto the cellulose fibres through a chemical co-precipitation method to make the fibre magnetic. In the presence of a magnetic field, the fibres became oriented within the scaffold. The efficacy of scaffolds for bone repair are closely related to their microstructure [50,51]. By testing the tensile and compression properties of the fibre-oriented scaffolds in different directions, we concluded that the tensile and compression properties of the scaffolds in different directions were anisotropic. At the same time, the tensile strength and compressive strength perpendicular to the fibre direction
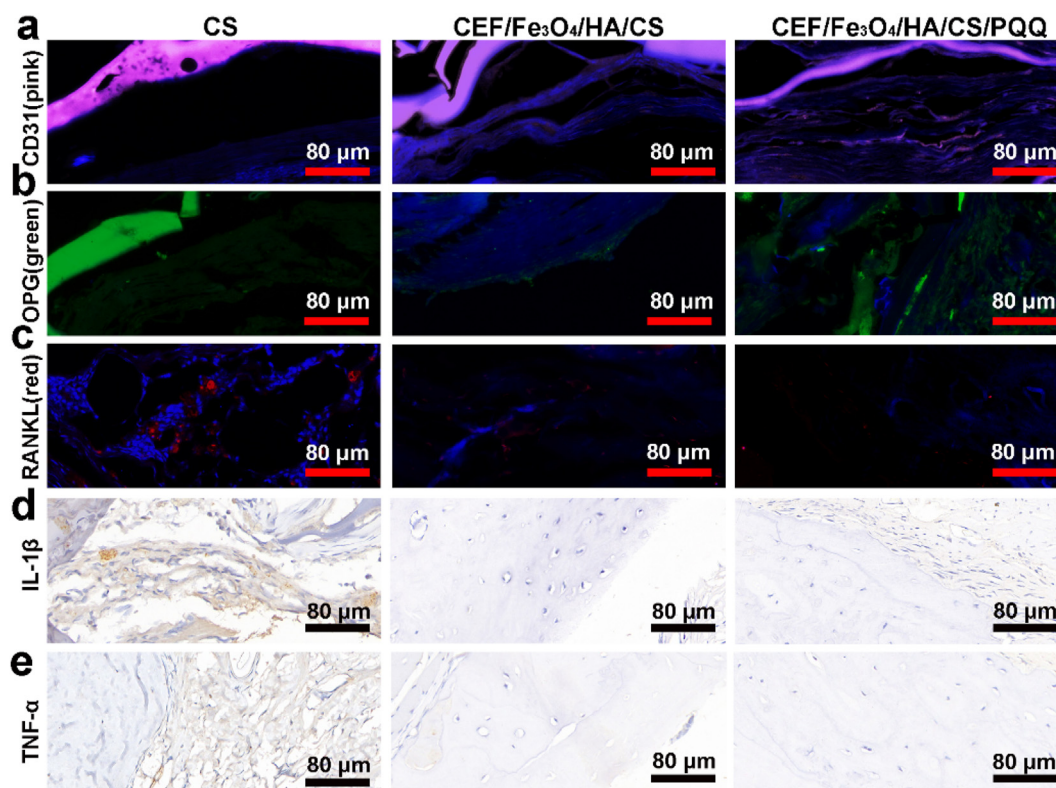

Fig. 10. (a, b, c) immunofluorescence for OPG, RANKL and CD31; (d, e) immunohistochemistry for TNF-α and IL-1β inflammatory factors.

were the highest, reaching 6.53 MPa and 1.53 MPa, respectively (Fig. 4). This result proves our conjecture and provides a new approach for improving the mechanical properties of scaffolds.

In addition, the arrangement of cellulose fibres with an oriented structure was consistent with the arrangement direction of the extracellular matrix of the bone tissue. Most of the extracellular matrix is composed of collagen fibres and hydroxyapatite. Therefore, we deposited nano-hydroxyapatite particles on the cellulose fibres to prepare oriented cellulose fibres (Fig. 1g and h). In this way, cellulose fibres with nano-hydroxyapatite particles were oriented and arranged on the surface of chitosan. Inspired by the "solid" structure of mollusc nacre, a nacre-mimicking HA/CS-layered scaffold was fabricated in our previous work. The CEF/Fe$_3$O$_4$/HA/CS layered scaffold in this study was prepared as a biological scaffold with a layered structure (Fig. 2a and d). Thus, the strength of the biomaterial could be further enhanced. Moreover, the CEF/Fe$_3$O$_4$/HA/CS-layered scaffold was more beneficial for cell invasion and migration. In addition, we added an inhibitor of the NF-κB pathway (PQQ) to the nano-hydroxyapatite voids on the surface of the cellulose fibres, which inhibited the acute inflammatory response and osteoclast differentiation. When examining drug release from the scaffolds, we found that the release rate was faster in the early stage, while a slow release was observed later. The drug concentration during early release did not produce toxic responses in the cells.

The CEF/Fe$_3$O$_4$/HA/CS/PQQ layered scaffolds solved the challenge regarding the biological strength of the scaffold [31,32,35]. It can simultaneously promote bone regeneration, promote the formation of new blood vessels, and inhibit acute inflammatory responses. The extracellular matrix in bone tissue is mostly composed of hydroxyapatite and collagen fibers. Therefore, we deposited nano-hydroxyapatite on cellulose fibres with an oriented structure while loading anti-inflammatory inhibitors.

When the CEF/Fe$_3$O$_4$/HA/CS/PQQ layered scaffold fills a bone defect, it mimics an implant in the human body. Owing to trauma during an operation, bone defects are bound to cause an acute inflammatory reaction. The early acute inflammatory response leads to the aggregation of macrophages and the release of inflammatory factors, thereby affecting the differentiation and mineralisation of osteoblasts. The CEF/Fe$_3$O$_4$/HA/CS/PQQ layered scaffold resolved the early acute inflammatory response, and its slow sustained release further regulated osteoclast generation in the later stage. This acute inflammatory response was inhibited when the PQQ inhibitor was released from the interior of the nano-hydroxyapatite on the cellulose fibres (Fig. 10d and e).

Bone tissue contains osteocytes, osteoblasts, and osteoclasts. Differentiation of osteoclasts from macrophages. Osteoblast bone resorption and regeneration are involved in the regulation of bone homeostasis. The OPG/RANKL system plays a key role in regulating bone homeostasis. The OPG and RANKL proteins are expressed on the membranes of osteocytes and osteoblasts, regulating osteoclast differentiation. Moreover, osteoclast differentiation is enhanced by the action of inflammatory factors. Subsequent studies have investigated osteoclast differentiation. Western blotting showed that p–NF–κB was inhibited, and the number of TRAP-positive cells was significantly reduced (Fig. 7a, j). Animal experiments showed that the trend of OPG protein fluorescence intensity was CEF/Fe$_3$O$_4$/HA/CS/PQQ > CEF/Fe$_3$O$_4$/HA/CS > CS; however, the trend of fluorescence intensity of RANKL protein was the opposite (Fig. 10a and b). These results showed that the CEF/Fe$_3$O$_4$/HA/CS/PQQ layered scaffold could inhibit the acute inflammatory response and regulate bone homeostasis in the early stage.

Subsequent experiments were then conducted on bone regeneration and the promotion of neovascularisation. Scanning electron microscopy (Fig. 6d) revealed that osteoblasts adhered to the surface of the oriented cellulose fibres. Many nano-hydroxyapatite components were also deposited on the surface of the oriented cellulose fibres, which also accelerated the mineralisation and differentiation of osteoblasts (Fig. 6c, f). The oriented structure of the layered scaffolds not only improved their mechanical strength but also promoted the growth of collagen fibres along its structure. In addition, when we created the animal model, we removed the periosteum to avoid intraperitoneal osteogenesis and focused on endochondral osteogenesis. Collagen fibres, when accompanied by oriented cellulose fibres, were further transformed into cartilage under the action of nano-hydroxyapatite, finally ossifying into new bone tissue. This was why the protein expressions of BMP-2, RUNX-2, and OPN were increased in the CEF/Fe$_3$O$_4$/HA/CS/PQQ group and CEF/Fe$_3$O$_4$/HA/CS group (Fig. 9g). Furthermore, we found that the CEF/Fe$_3$O$_4$/HA/CS/PQQ and CEF/Fe$_3$O$_4$/HA/CS layered scaffolds also accelerated angiogenesis through cell tube formation experiments *in vitro* (Fig. 8b). Immunofluorescence analysis also revealed that the protein expression of CD31, an indicator of neovascularisation, was enhanced in the groups containing layered scaffolds (Fig. 10c).

5. Conclusions

To address the difficulty in inducing endochondral osteogenesis (*in situ* bone regeneration), we successfully prepared magnetically oriented cellulose fibres and deposited nano-hydroxyapatite on cellulose fibres as drug-loading particles (CEF/Fe$_3$O$_4$/HA/CS). We then loaded the small-molecule inhibitor PQQ inside the nano-hydroxyapatite on the magnetically oriented cellulose fibres, finally fabricating CEF/Fe$_3$O$_4$/HA/CS/PQQ scaffolds with a layered structure. The CEF/Fe$_3$O$_4$/HA/CS/PQQ scaffolds showed layered macropores with sizes of 100–200 μm. Nano-hydroxyapatite was deposited on the cellulose fibres, which were oriented and arranged on the surface of the layered chitosan. The CEF/Fe$_3$O$_4$/HA/CS/PQQ-layered scaffolds promoted the invasion and migration of osteoblasts, macrophages, and vascular endothelial cells. Fibres with oriented structures provided adhesion sites for osteoblasts and vascular endothelial cells. Then, collagen fibres also grew along the direction of the oriented fibres, finally forming endochondral bone. When macrophages migrated onto the fibres, PQQ inhibited the release of inflammatory factors (IL-1β and TNF-α) from the macrophages by inhibiting the activation of the NF-κB signalling pathway and the differentiation of macrophages into osteoclasts. In conclusion, fibres with an oriented structure can promote the migration of vascular endothelial cells, accelerate the formation of new blood vessels, and provide sufficient nutrition for endochondral ossification.

Credit author statement

CQZ and YPG provided guidance for this study and designed the specific procedures of the trial. QFK and WTJ wrote the manuscript. YWG, ZYZ and MC completed the specific process of the experiment.

Ethics approval statement

All animal experiments were approved by the Animal Research Committee of Shanghai Jiao Tong University Affiliated Sixth People's Hospital (approval number: SYXK2011-0128; January 1, 2011 Shanghai, China).

Declaration of competing interest

The authors declare that they have no known competing financial interests or personal relationships that could have appeared to influence the work reported in this paper.

Data availability

Data will be made available on request.

References

[1] M.T. Dahl, S. Morrison, Segmental bone defects and the history of bone transport, J. Orthop. Trauma 35 (Suppl 4) (2021) S1–S7.
[2] R. Dimitriou, E. Jones, D. McGonagle, P.V. Giannoudis, Bone regeneration: current concepts and future directions, BMC Med. 9 (2011) 66.
[3] A.N. Ball, S.W. Donahue, S.J. Wojda, C.W. McIlwraith, C.E. Kawcak, N. Ehrhart, L.R. Goodrich, The challenges of promoting osteogenesis in segmental bone defects and osteoporosis, J. Orthop. Res. 36 (6) (2018) 1559–1572.
[4] C.K. Cheng, X.H. Wang, Y.C. Luan, N.Z. Zhang, B.L. Liu, X.Y. Ma, M.D. Nie, Challenges of pre-clinical testing in orthopedic implant development, Med. Eng. Phys. 72 (2019) 49–54.
[5] O. Pieske, A. Wittmann, J. Zaspel, T. Loffler, B. Rubenbauer, H. Trentzsch, S. Piltz, Autologous bone graft versus demineralized bone matrix in internal fixation of ununited long bones, J. Trauma Manag. Outcome 3 (2009) 11.
[6] J.H. Zeng, S.W. Liu, L. Xiong, P. Qiu, L.H. Ding, S.L. Xiong, J.T. Li, X.G. Liao, Z.M. Tang, Scaffolds for the repair of bone defects in clinical studies: a systematic review, J. Orthop. Surg. Res. 13 (1) (2018) 33.
[7] J. Revuelta, I. Fraile, D.T. Monterrey, N. Pena, R. Benito-Arenas, A. Bastida, A. Fernandez-Mayoralas, E. Garcia-Junceda, Heparanized chitosans: towards the third generation of chitinous biomaterials, Mater. Horiz. 8 (10) (2021) 2596–2614.
[8] X. Zhou, N. Zhang, S. Mankoci, N. Sahai, Silicates in orthopedics and bone tissue engineering materials, J. Biomed. Mater. Res. 105 (7) (2017) 2090–2102.
[9] H. Chouirfa, H. Bouloussa, V. Migonney, C. Falentin-Daudre, Review of titanium surface modification techniques and coatings for antibacterial applications, Acta Biomater. 83 (2019) 37–54.
[10] J.S. Fernandes, P. Gentile, R.A. Pires, R.L. Reis, P.V. Hatton, Multifunctional bioactive glass and glass-ceramic biomaterials with antibacterial properties for repair and regeneration of bone tissue, Acta Biomater. 59 (2017) 2–11.
[11] A. Bharadwaz, A.C. Jayasuriya, Recent trends in the application of widely used natural and synthetic polymer nanocomposites in bone tissue regeneration, Mater Sci Eng C Mater Biol Appl 110 (2020), 110698.
[12] P. Wang, L. Zhao, J. Liu, M.D. Weir, X. Zhou, H.H. Xu, Bone tissue engineering via nanostructured calcium phosphate biomaterials and stem cells, Bone Res 2 (2014), 14017.
[13] Y.W. Ge, J.W. Lu, Z.Y. Sun, Z.Q. Liu, J. Zhou, Q.F. Ke, Y.Q. Mao, Y.P. Guo, Z.A. Zhu, Ursolic acid loaded-mesoporous bioglass/chitosan porous scaffolds as drug delivery system for bone regeneration, Nanomedicine 18 (2019) 336–346.
[14] L.L. Hench, I. Thompson, Twenty-first century challenges for biomaterials, J. R. Soc. Interface 7 (Suppl 4) (2010) S379–S391.
[15] Y.-W.G. Pei-Pei Zhao, Xiao-Liang Liu, Ke Qin-Fei, Jing-Wei Zhang, Zhen-An Zhu, Ya-Ping Guo, Ordered arrangement of hydrated GdPO4 nanorods in magnetic chitosan matrix promotes tumor photothermal therapy and bone regeneration against breast cancer bone metastases, Chem. Eng. J. 381 (2020), 122694.
[16] C.V. Rodrigues, P. Serricella, A.B. Linhares, R.M. Guerdes, R. Borojevic, M.A. Rossi, M.E. Duarte, M. Farina, Characterization of a bovine collagen-hydroxyapatite composite scaffold for bone tissue engineering, Biomaterials 24 (27) (2003) 4987–4997.
[17] S. Pitaru, S. Kotev-Emeth, D. Noff, S. Kaffuler, N. Savion, Effect of basic fibroblast growth factor on the growth and differentiation of adult stromal bone marrow cells: enhanced development of mineralized bone-like tissue in culture, J. Bone Miner. Res. 8 (8) (1993) 919–929.
[18] X. Luo, S. Zhang, B. Luo, H. Li, Engineering collagen fiber templates with oriented nanoarchitecture and concerns on osteoblast behaviors, Int. J. Biol. Macromol. 185 (2021) 77–86.
[19] M. Green, D.H. Isaac, G.M. Jenkins, Bone microstructure by collagenase etching, Biomaterials 6 (3) (1985) 150–152.
[20] R. Khanna, K.S. Katti, D.R. Katti, Bone nodules on chitosan-polygalacturonic acid-hydroxyapatite nanocomposite films mimic hierarchy of natural bone, Acta Biomater. 7 (3) (2011) 1173–1183.
[21] E.S. Lai, C.M. Anderson, G.G. Fuller, Designing a tubular matrix of oriented collagen fibrils for tissue engineering, Acta Biomater. 7 (6) (2011) 2448–2456.
[22] A.M. Ferreira, P. Gentile, V. Chiono, G. Ciardelli, Collagen for bone tissue regeneration, Acta Biomater. 8 (9) (2012) 3191–3200.
[23] R.B. Montero, X. Vial, D.T. Nguyen, S. Farhand, M. Reardon, S.M. Pham, G. Tsechpenakis, F.M. Andreopoulos, bFGF-containing electrospun gelatin scaffolds with controlled nano-architectural features for directed angiogenesis, Acta Biomater. 8 (5) (2012) 1778–1791.
[24] B. Wang, Q. Cai, S. Zhang, X. Yang, X. Deng, The effect of poly (L-lactic acid) nanofiber orientation on osteogenic responses of human osteoblast-like MG63 cells, J. Mech. Behav. Biomed. Mater. 4 (4) (2011) 600–609.
[25] M.A. Accardi, S.D. McCullen, A. Callanan, S. Chung, P.M. Cann, M.M. Stevens, D. Dini, Effects of fiber orientation on the frictional properties and damage of regenerative articular cartilage surfaces, Tissue Eng. 19 (19–20) (2013) 2300–2310.
[26] C. Liu, C. Zhu, J. Li, P. Zhou, M. Chen, H. Yang, B. Li, The effect of the fibre orientation of electrospun scaffolds on the matrix production of rabbit annulus fibrosus-derived stem cells, Bone Res 3 (2015), 15012.
[27] S. Yang, X. Shi, X. Li, J. Wang, Y. Wang, Y. Luo, Oriented collagen fiber membranes formed through counter-rotating extrusion and their application in tendon regeneration, Biomaterials 207 (2019) 61–75.
[28] J.A. Matthews, G.E. Wnek, D.G. Simpson, G.L. Bowlin, Electrospinning of collagen nanofibers, Biomacromolecules 3 (2) (2002) 232–238.
[29] A.A. Salifu, C. Lekakou, F. Labeed, Multilayer cellular stacks of gelatin-hydroxyapatite fiber scaffolds for bone tissue engineering, J. Biomed. Mater. Res. 105 (3) (2017) 779–789.
[30] H. Bai, F. Walsh, B. Gludovatz, B. Delattre, C. Huang, Y. Chen, A.P. Tomsia, R.O. Ritchie, Bioinspired hydroxyapatite/poly(methyl methacrylate) composite with a nacre-mimetic architecture by a bidirectional freezing method, Adv. Mater. 28 (1) (2016) 50–56.
[31] R.L. Yang, Y.J. Zhu, F.F. Chen, D.D. Qin, Z.C. Xiong, Bioinspired macroscopic ribbon fibers with a nacre-mimetic architecture based on highly ordered alignment of ultralong hydroxyapatite nanowires, ACS Nano 12 (12) (2018) 12284–12295.
[32] S. Xia, Z. Wang, H. Chen, W. Fu, J. Wang, Z. Li, L. Jiang, Nanoasperity: structure origin of nacre-inspired nanocomposites, ACS Nano 9 (2) (2015) 2167–2172.
[33] Y.W. Ge, Z.H. Fan, Q.F. Ke, Y.P. Guo, C.Q. Zhang, W.T. Jia, SrFe12O19-doped nano-layered double hydroxide/chitosan layered scaffolds with a nacre-mimetic architecture guide in situ bone ingrowth and regulate bone homeostasis, Mater Today Bio 16 (2022), 100362.
[34] C.J. Zhang, C. Hu, Q.F. Ke, C.X. Guo, Y.J. Guo, Y.P. Guo, Nacre-inspired hydroxyapatite/chitosan layered composites effectively remove lead ions in continuous-flow wastewater, J. Hazard Mater. 386 (2020), 121999.
[35] H. Zhao, L. Guo, Nacre-inspired structural composites: performance-enhancement strategy and perspective, Adv. Mater. 29 (45) (2017).
[36] S. Qiu, X. Ren, X. Zhou, T. Zhang, L. Song, Y. Hu, Nacre-inspired black phosphorus/nanofibrillar cellulose composite film with enhanced mechanical properties and superior fire resistance, ACS Appl. Mater. Interfaces 12 (32) (2020) 36639–36651.
[37] J. Medinger, M. Nedyalkova, T. Furlan, J. Luthi, J. Hofmann, A. Neels, M. Lattuada, Preparation and machine-learning methods of nacre-like composites from the self-assembly of magnetic colloids exposed to rotating magnetic fields, Acs Appl Mater Inter 13 (40) (2021) 48040–48052.
[38] Q. Geng, H. Gao, R. Yang, K. Guo, D. Miao, Pyrroloquinoline quinone prevents estrogen deficiency-induced osteoporosis by inhibiting oxidative stress and osteocyte senescence, Int. J. Biol. Sci. 15 (1) (2019) 58–68.
[39] Q. Zhou, H. Jin, N. Shi, S. Gao, X. Wang, S. Zhu, M. Yan, Inhibit inflammation and apoptosis of pyrroloquinoline on spinal cord injury in rat, Ann. Transl. Med. 9 (17) (2021) 1360.
[40] C. Huang, D. Ming, W. Wang, Z. Wang, Y. Hu, X. Ma, F. Wang, Pyrroloquinoline quinone alleviates jejunal mucosal barrier function damage and regulates colonic microbiota in piglets challenged with enterotoxigenic Escherichia coli, Front. Microbiol. 11 (2020) 1754.
[41] T. Kumazawa, T. Hiwasa, M. Takiguchi, O. Suzuki, K. Sato, Activation of Ras signaling pathways by pyrroloquinoline quinone in NIH3T3 mouse fibroblasts, Int. J. Mol. Med. 19 (5) (2007) 765–770.
[42] K. Saihara, R. Kamikubo, K. Ikemoto, K. Uchida, M. Akagawa, Pyrroloquinoline quinone, a redox-active o-quinone, stimulates mitochondrial biogenesis by activating the SIRT1/PGC-1alpha signaling pathway, Biochemistry 56 (50) (2017) 6615–6625.
[43] L. Zhang, J. Liu, C. Cheng, Y. Yuan, B. Yu, A. Shen, M. Yan, The neuroprotective effect of pyrroloquinoline quinone on traumatic brain injury, J. Neurotrauma 29 (5) (2012) 851–864.
[44] Y. Wu, M. Zhao, Z. Lin, Pyrroloquinoline quinone (PQQ) alleviated sepsis-induced acute liver injury, inflammation, oxidative stress and cell apoptosis by downregulating CUL3 expression, Bioengineered 12 (1) (2021) 2459–2468.
[45] T. Wu, S. Yu, D. Chen, Y. Wang, Bionic design, materials and performance of bone tissue scaffolds, Materials 10 (10) (2017).
[46] M. Ghetti, H. Topouzi, G. Theocharidis, V. Papa, G. Williams, E. Bondioli, G. Cenacchi, J.T. Connelly, C.A. Higgins, Subpopulations of dermal skin fibroblasts

secrete distinct extracellular matrix: implications for using skin substitutes in the clinic, Br. J. Dermatol. 179 (2) (2018) 381–393.

[47] K.Y. Ching, O.G. Andriotis, S. Li, P. Basnett, B. Su, I. Roy, R.S. Tare, B.G. Sengers, M. Stolz, Nanofibrous poly(3-hydroxybutyrate)/poly(3-hydroxyoctanoate) scaffolds provide a functional microenvironment for cartilage repair, J. Biomater. Appl. 31 (1) (2016) 77–91.

[48] A.G. Guex, F.M. Kocher, G. Fortunato, E. Korner, D. Hegemann, T.P. Carrel, H.T. Tevaearai, M.N. Giraud, Fine-tuning of substrate architecture and surface chemistry promotes muscle tissue development, Acta Biomater. 8 (4) (2012) 1481–1489.

[49] M. Horbens, M. Eder, C. Neinhuis, A materials perspective of Martyniaceae fruits: exploring structural and micromechanical properties, Acta Biomater. 28 (2015) 13–22.

[50] T.A. Grunewald, M. Liebi, N.K. Wittig, A. Johannes, T. Sikjaer, L. Rejnmark, Z. Gao, M. Rosenthal, M. Guizar-Sicairos, H. Birkedal, M. Burghammer, Mapping the 3D orientation of nanocrystals and nanostructures in human bone: indications of novel structural features, Sci. Adv. 6 (24) (2020), eaba4171.

[51] Q.-Y.W. Ya-Qi Tang, K. Qin-Fei, Chang-Qing Zhang, Ya-Ping Guo Jun-Jie Guan, Mineralization of ytterbium-doped hydroxyapatite nanorod arrays in magnetic chitosan scaffolds improves osteogenic and angiogenic abilities for bone defect healing, Chem. Eng. J. 387 (2020), 124166.